

Energy-dependent conduction band mass of SiO₂ determined by ballistic electron emission microscopy

R. Ludeke^{a)}

IBM T. J. Watson Research Center, Yorktown Heights, New York 10598

Andreas Schenk

Integrated Systems Laboratory, Swiss Federal Institute of Technology, Gloriastrasse 35, CH-8092 Zürich, Switzerland

(Received 19 January 1999; accepted 5 May 1999)

Quantum interference oscillations in ballistic electron emission microscopy (BEEM) spectra were observed for metal–oxide–semiconductor structures with 23 and 30 Å SiO₂ interlayers. Maxima in the transmission coefficients, obtained from solutions of the one-dimensional Schrödinger equation that included image force corrections, could be matched to the spectral maxima provided that the effective electron mass m_{ox} , an adjustable parameter, was increased at each of the consecutive higher energy maxima. The resulting energy dependence or dispersion of $m_{\text{ox}}(E)$ showed a dependence on the oxide thickness. The 23 and 30 Å oxides exhibit initial (zero kinetic energy) m_{ox} values of $0.52 m_0$ and $0.45 m_0$, respectively, that disperse upward with energy by $\approx 0.3 m_0$ over a 0–2.5 eV range in kinetic energies. The range of m_{ox} values observed is substantially lower than the average m_{ox} values deduced from quantum interference in Fowler–Nordheim tunneling experiments. The origin of these differences are discussed, and it is argued that BEEM is an inherently simpler and less error prone technique to evaluate m_{ox} . © 1999 American Vacuum Society. [S0734-211X(99)05004-0]

I. INTRODUCTION

The effective mass m_{ox} of the conduction band electrons in amorphous SiO₂ is a relevant parameter in the prediction of hot electron effects in metal–oxide–semiconductor (MOS) structures, as well as in performance simulations of field effect transistors.¹ Nevertheless, its value has been contentious over decades, a problem derived from its relegation to a fitting parameter that is used to force agreement of frequently over simplified transport equations with experiment. Moreover, few attempts have been made to assess the consequences of the physical constraints imposed in the data interpretation and their resulting impact on m_{ox} . As a result the reported values for m_{ox} ranged from a low of $0.3 m_0$,² where m_0 is the free electron mass, to estimates as high as $0.85 m_0$.^{3,4} An underlying but never stated premise in all measurements reported thus far is the assumption of an energy independent or dispersionless mass. This assumption, as we shall see shortly, is a consequence of the inability to extract a dispersive m_{ox} with conventional transport techniques. The current–voltage (I – V) measurements give instead values of m_{ox} averaged over an energy range determined by the experiment. In this work we present an approach based on quantum interference effects of electrons injected directly into the conduction band of SiO₂ from which it is possible to derive the energy dispersion of m_{ox} .

The most commonly employed I – V transport measurement of MOS capacitor structures is Fowler–Nordheim (FN) tunneling, in which a sufficiently high potential V_{ox} is applied across the oxide to field-inject electrons via tunneling from near the Fermi level of the gate and thence into the

conduction band of the SiO₂. This is schematically shown in the top illustration of Fig. 1. The electron, represented by a plane wave, tunnels through the trapezoidal barrier represented by the solid line and emerges in the conduction band of the SiO₂. There it continues to gain energy due to field acceleration as it approaches the SiO₂–Si interface. The current density is given by the well known FN expression obtained in the Wentzel–Kramers–Brillouin (WKB) approximation,⁵ $J_{\text{FN}} \propto \exp[-4(2 m_{\text{ox}})^{1/2} \Phi_B^{3/2} d_{\text{ox}} / 3\hbar V_{\text{ox}}]$, where Φ_B is the barrier height, d_{ox} the oxide thickness, and V_{ox} the net oxide potential. Experimental I – V curves are generally fitted to this simple relationship, with the assumption that both Φ_B and V_{ox} are known, but not m_{ox} , which thereby is treated as a fitting parameter. This expression for J_{FN} ignores screening effects arising from the presence of the interfaces, an intentional omission based on results for thicker oxides.⁶ For ultrathin oxides (<10 nm) these effects, expressed through the classical concept of image force lowering of the barrier and illustrated by the dashed line in Fig. 1(a), cannot be ignored.^{7,8} The inclusion of image force effects requires a numerical solution for J_{FN} , whether represented in terms of a complete Schrödinger equation, or as an approximation, such as WKB.⁷ The mass deduced from fits is that of a particle tunneling through the barrier, with a value that should represent the effective mass of the imaginary branch of the band structure. It is expected to be different from the real conduction band mass, although at the band edge their values should be nearly equal. However, the electron is constantly changing its energy from the point of injection to its emergence in the conduction band (a change exceeding 3 eV), yet it is assumed that its mass is either constant or that the deduced mass represents an energy av-

^{a)}Electronic mail: ludeke@watson.ibm.com

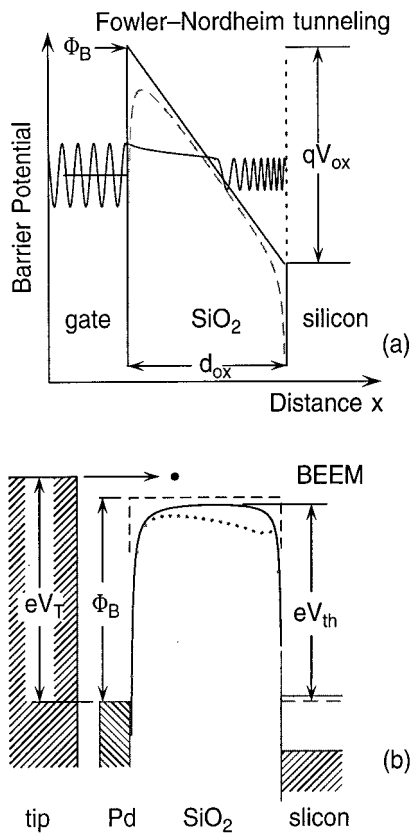


FIG. 1. (a) Energy diagram for FN tunneling is shown at the top under the usual assumption of a trapezoidal barrier that neglects image force effects. The influence of the latter is shown by the dashed curve (b) A corresponding diagram for a BEEM experiment. The barrier potential is shown with (solid) and without (dashed) image force corrections. Φ_B is the potential difference between the Fermi level of the metal and the SiO₂ conduction band minimum. eV_{th} represents the barrier height with the inclusion of image force lowering and corresponds to the threshold energy for current detection measured in a BEEM spectrum. V_T is the STM bias and corresponds to the kinetic energy of the electrons injected into the metal gate. The dotted potential represents the consequence of positive oxide charge near the SiO₂-Si interface.

eraged value. The same can be said of its mass in the conduction band, as the electron is accelerated towards the SiO₂-Si interface. The mass, the real m_{ox} , can also be obtained in a FN experiment from weak oscillations in J_{FN} . Such oscillatory structure arising from interference of the electron wave function in the “cavity” between the conduction band edge and the SiO₂-Si interface was predicted by Gundlach,⁹ and first observed by Maserjian and Petersson,^{3,10} and subsequently by others.^{4,11-14} The experimental reality of a changing electron energy and its complications, together with the inherently weak oscillatory structure modulating a large background current, makes the technique unsuitable for measuring mass changes with electron energy. Band structure calculations indicate that for crystalline quartz considerable deviations from parabolicity occur within 1–2 eV of the lower band edge, with additional bands starting to contribute to the density of states near these energies.¹⁵⁻¹⁷ However, the conduction bands are often inadequately treated in such calculations and it is therefore difficult to extract an accurate

dispersion of m_{ox} . Theoretical estimates of m_{ox} for α -quartz range from $m_{ox} = 0.3^{16}$ to $0.5 m_0^{17}$. Even if accurate values of m_{ox} and their dispersions were calculated for the polyphases of crystalline quartz, a direct correspondence to amorphous quartz would still be speculative, although it has been argued that on the short range scale of a few nanometers the distorted amorphous phase still exhibits many band-like properties akin to crystalline SiO₂.¹

Quantum interference oscillations have recently been observed in the I - V spectrum of electrons injected directly into the conduction band of SiO₂.¹⁸ The technique, ballistic electron emission microscopy or BEEM, uses the tip of a scanning tunneling microscope (STM) to inject electrons into the thin metal gate of a MOS structure, whence they proceed ballistically to enter the SiO₂ and subsequently the Si substrate. They emerge from the Si as a collector current that is modulated by the interference phenomenon in the oxide. For over-the-barrier transmission, maxima in the transmission probability for a rectangular barrier (i.e., in the absence of an internal oxide potential V_{ox}) occur at the following energies:⁹

$$E = (n\pi\hbar/d_{ox})^2/2m_{ox} \quad \text{with } n = 1, 2, 3, \dots, \quad (1)$$

from which m_{ox} can be deduced by matching theoretical maxima to those obtained experimentally. However, the presence of an internal field plus the inclusion of image force effects requires that the equations be solved numerically. Using such an approach, a value of $m_{ox} = (0.63 \pm 0.09)m_0$ was obtained for a 2.8 nm oxide.¹⁸ Subsequent improvements in the data quality have now necessitated the inclusion of an energy dependent mass to match experiment with theory, which is the topic of this article.

II. EXPERIMENTAL DETAILS

A. Ballistic electron emission microscopy/spectroscopy

BEEM, as mentioned earlier, is a STM based microscopy that differs from conventional STM by the presence of a thin metal layer deposited on a substrate, in the present case a SiO₂-Si sample. The only purpose of the metal layer is to provide a reference electrode relative to which the STM tip is biased with a potential V_T . The electrons injected into the metal layer by the STM tip thus have an energy of eV_T . The thickness of the metal should be comparable or preferably less than the electron mean free path in the metal, so that the electrons can traverse the layer ballistically. If their energy is larger than the potential barrier posed by the oxide—in the present case the potential Φ_B representing the difference between the Fermi level in the metal and the bottom of the SiO₂ conduction band—some electrons will be injected into the conduction band, and after traversing the oxide and entering the Si, will emerge as a collector current I_c from the substrate. An energy diagram for a BEEM experiment at zero applied bias is shown at the bottom of Fig. 1. The probability for the electron to reach the Si is dependent on the overlap of the conduction band density of states at the interfaces, the transmission probability $T_{ox}(E)$ across the oxide, as well as transmission probabilities of a quantum mechanical origin

(e.g., transverse momentum conservation). These issues have been discussed elsewhere.^{1,7,19} Although for oxide films thicker than about 4 nm T_{ox} is strongly dependent on electron-phonon scattering,^{19,20} for the thinner oxides used here this scattering mechanism is not dominant, a conclusion supported by the observation of interference phenomena. Consequently, scattering will be ignored in our analysis of T_{ox} .

In the present application BEEM is exclusively used in the spectroscopy mode, in which the raster scan of the STM is stopped and the collector current I_c is measured as V_T is ramped over a range that includes the barrier potential Φ_B . I_c becomes finite once V_T exceed Φ_B , or more precisely, Φ_B modified by the image potential and any oxide potential that affects the net barrier height. The consequence of the image force is included in the potential shown in Fig. 1(b) (solid line), the dashed line representing the bare potential. The STM is generally operated at a constant tunneling current I_T . An important experimental consideration is tip drift, which should be negligible over the acquisition time for a spectrum, which is typically ~ 1.5 min. We waited until tip drifts were below 1 Å/min before attempting the acquisition of spectra.

B. Sample preparation

Device-grade amorphous SiO₂ layers were thermally grown in dry oxygen at 800 °C. The substrates were 125 mm diameter Si(100) wafers, boron doped in the low 10^{16} cm⁻³ range. No additional treatments were performed after the oxidation. The thickness d_{ox} of the oxides studied in this work were 23 and 30 Å. The thickness was determined with an ellipsometer, and represents an average of over 50 measurements over the wafer. All measurements were within 1 Å of the averaged value. The thickness of the oxides was also obtained from capacitance–voltage (C – V) measurements, using 500-Å-thick W dots deposited *ex situ* by chemical vapor deposition. Their values were 1 Å less than those obtained ellipsometrically for oxides of thicknesses in the 20–40 Å range. We chose the ellipsometric values for the data analysis, as the C – V data reduction routines included corrections that were unnecessary for metal gates and which resulted in a small (~ 1 Å) underestimate of the thickness.

Approximately 8×15 mm² samples were cleaved from the wafers in a dry box. An ohmic contact was made by scraping a small droplet of a Ga–In alloy into the backside of the samples. They were then introduced into an ultrahigh vacuum (UHV) preparation chamber, where each sample, prior to metallization, was annealed separately near 250 °C for 10 h to remove water and other volatile surface contaminants. Arrays of metal dots, 0.2 mm in diameter, were deposited by evaporating the metal through a shadow mask. The samples were cooled to a temperature of ~ 30 K in order to minimize surface diffusion and thereby achieve pinhole-free layers at the lowest possible coverages. For Pd, which was used for the 23 Å oxide, full coverage was achieved in the 30–40 Å range. The resulting morphology, shown in Fig. 2(a), consists of nodules typically 80 Å in diameter that protruded < 10 Å above the valleys. Tungsten was used for the

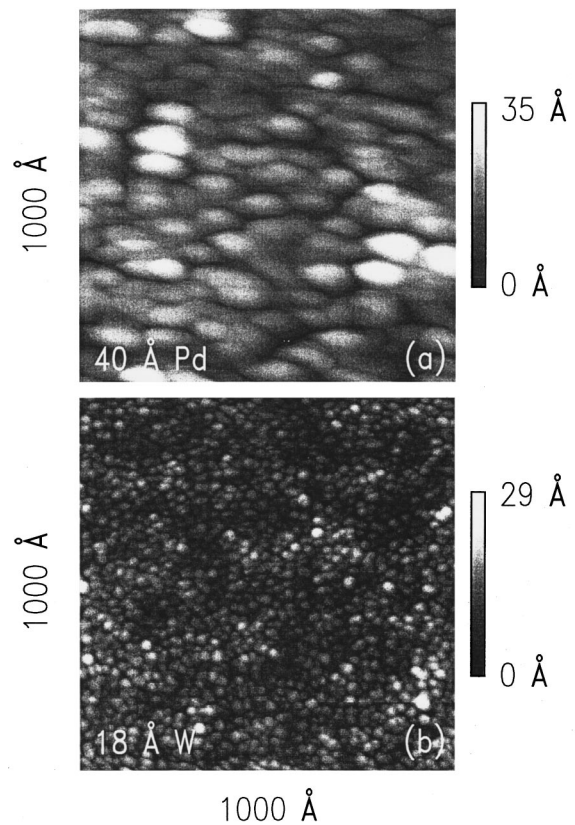


FIG. 2. 1000×1000 Å² topographic images for metal on SiO₂: (a) 40 Å Pd film and (b) 18 Å W film. Both films were deposited with the SiO₂/Si substrate near 30 K.

30 Å oxide sample. It was evaporated from a low voltage and low power (< 1800 V, ~ 200 W) electron beam evaporator to minimize oxide damage, as well as to maintain a low chamber pressure during metallization ($\sim 10^{-8}$ Torr of mostly H₂). Pinhole-free films were obtained in the 15–18 Å range. The morphology of a W layer is shown in Fig. 2(b). Its nodular texture, which is substantially finer than that of Pd, exhibits a rather homogeneous distribution of grain sizes in the 15–20 Å range. The small size of the W grains serves to refocus on the importance of a low STM tip drift during the acquisition of a spectrum, as the tip position should be kept well within the area of the grain. Otherwise the curvature of the grain will cause undesirable changes in electron injection angle as the tip drifts near the grain boundary. It has been known for some time that the injection angle plays a critical role in the transmission.²¹ The finished sample was allowed to warm up to room temperature and was subsequently transferred under UHV into the STM chamber. A reference electrode at the STMs ground potential, needed to bias the tip, was carefully positioned onto a selected metal dot by means of three orthogonally mounted Inchworms™. After the STM tip reached tunneling the drift was checked repeatedly until it decayed to the desired level, usually in a few hours. Once stabilized, large lateral movement of the tip were avoided as well to minimize tip creep.

BEEM spectra were usually taken on previously unmeasured areas of the sample to avoid trap generation and charg-

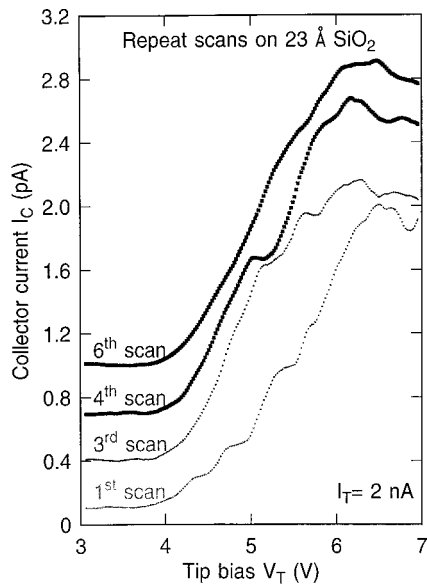


FIG. 3. BEEM spectra taken on the same location of a Pd/23 Å SiO₂/p-Si(100) MOS structure. The first scan was taken on a spot that had not been previously exposed to electrons of sufficient energy to inject electrons into the SiO₂. The quantum interference oscillations are substantially changed after repeat scans, being nearly obliterated after about 6 scans. The spectra show few additional changes beyond the sixth scan. The spectra are displaced vertically for clarity. $I_T=2$ nA.

ing from prior hot electron injections.²² Any oxide charge affects V_{ox} locally, thereby altering the interference structure, which renders a determination of m_{ox} nearly impossible.¹⁸ Adjacent measurement points were separated by at least 250 Å. In order to achieve flat band conditions (i.e., $V_{ox}=0$), a +0.3 V bias was applied to the Si for the W-“gated” 30 Å oxide structure. In the absence of an external bias, the Fermi level of the W is commensurate with the midgap energy of the Si at the SiO₂-Si interface.²³ In contrast, the Pd contacts to oxides grown on p-Si(100) did not require a bias to achieve flatband conditions, as our best estimate suggests $V_{ox} \approx 0$ in the absence of a bias.²² This fortuitous situation avoids biasing the thin 23 Å oxide layer. Even biases of ~ 0.1 V would have resulted in large (direct) tunneling currents for the metal dot size used here, which would have saturated the operational amplifier.

III. INTERFACE PHENOMENA: SPECTROSCOPIC RESULTS

A. 23 Å oxide

BEEM spectra for a 40 Å Pd/23 Å SiO₂/p-Si(100) MOS structure are shown in Fig. 3. The STM tunneling current was set at 2 nA. An oscillatory component in the collector current is clearly discernible in the spectrum labeled first scan, which corresponds to the first scan on a virgin part of the sample surface. In this set of spectra we repeated the scans several times at the same location. The second scan already shows structure shifted to slightly different energies. The fourth scan is altogether different, and in general, shows weaker structure, a tendency that continues with subsequent

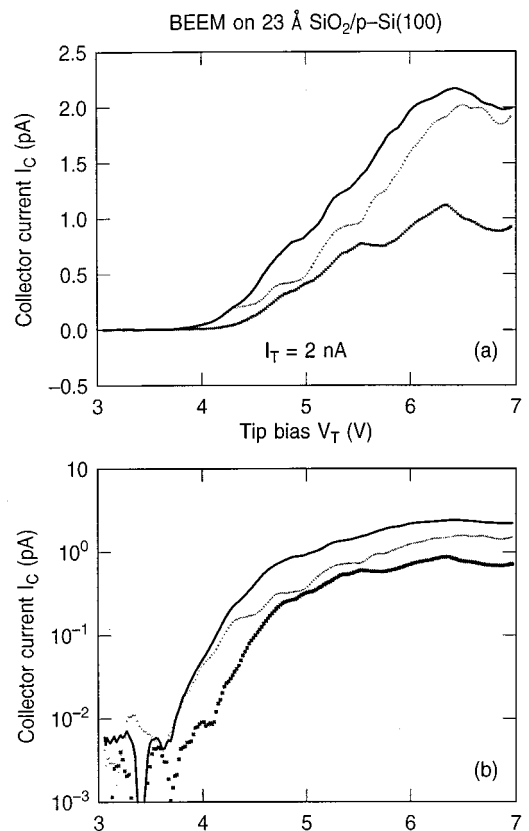


FIG. 4. BEEM spectra for a 40 Å Pd/23 Å SiO₂/p-Si(100) MOS structure. The bottom two curves are individual spectra, top curves are for an average of four spectra. Each spectrum was taken on a previously unexposed part of the higher energies. (b) Logarithmic plot of the same data as (a), which enhances the structure in the threshold region. $I_T=2$ nA.

scans, but does not change appreciably beyond the sixth scan shown in Fig. 3. We have observed this behavior on every occasion we performed repeated scans at a previously unexposed location of the surface. We generally observe a moderate increase in the collector current after the first and subsequent scans in the energy regions just above threshold. The increase is attributed to the generation of positive charge after the oxide layer has been electrically stressed with electrons of kinetic energy exceeding 2 eV ($V_T > |6|$ V).^{18,22} The positive charge near the Si interface lowers locally the barrier height, as depicted by the dotted barrier profile in Fig. 1(b). Noise in the spectra, which increases noticeably for $V_T > 5$ V, is an indication that charging and discharging events occur at trap sites generated by the hot electrons.²² Thus, it is important to realize that only the first spectrum may be representative of a charge free oxide region. Pre-existing traps in the oxide may also charge up and distort, or more likely obliterate the interference structure due to the inhomogeneous nature of the local fields. About 25% of the spectra show interference structure, but substantially fewer show relatively noise free characteristics over the whole spectral range from threshold, near 4 V, to the upper limit of 7 V.

Figure 4(a) depicts a couple of nearly identical spectra (the two lower curves) as well as an average over four spec-

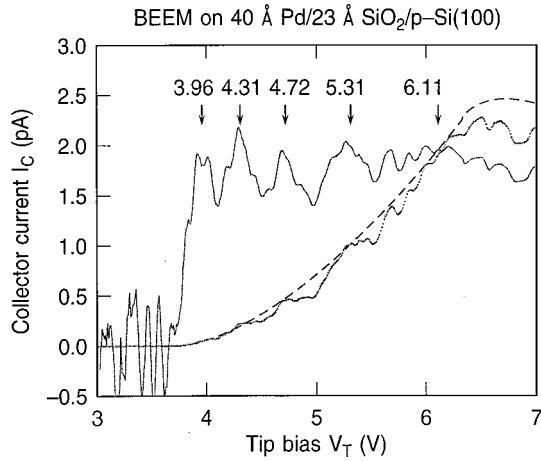


FIG. 5. Methodology for extracting interference maxima from BEEM spectra for a 23 Å oxide: a power law curve (dashed curve) is tangentially fitted to the experimental curve near the maxima. Their ratio simulates the transmission probability function, from which the indicated peak positions are easily obtained.

tra (upper curve). Whereas the oscillation are clearly discernible above 4.5 V in the linear plot, the structure below this value are more readily seen in a logarithmic plot, shown in Fig. 4(b) for the same spectra. To extract the energy location of the interference maxima, we have used a simple approach that assumes $I_c(V_T) = \bar{I}_c T_{ox}$, where \bar{I}_c is the collector current in the absence of interference. It can be simulated by fitting a smooth polynomial expression to the maxima of the experimental spectrum, as shown by the dashed line in Fig. 5. An “experimental” T_{ox} is then obtained by numerical division of I_c by \bar{I}_c as depicted in Fig. 5. The peak positions of the interference maxima are readily extracted from this curve with an accuracy of ± 0.02 V. Their values are shown above the maxima, and will be used in Sec. V to determine the effective mass.

B. 30 Å oxide

The tungsten metallization of a MOS structure on *p*-type Si results in an increase in the effective barrier height that reaches a maximum at the SiO₂-Si interface. In order to achieve flat band conditions it is therefore necessary to apply a positive oxide bias of 0.3 V to the substrate.²³ The resulting direct tunneling current of ~ 20 pA did not affect the BEEM spectrum and could be readily subtracted from the data. An exceptionally clean spectrum is shown in Fig. 6. As with the 23 Å oxide layer, about a quarter of the spectra showed interference oscillations, but only a fraction of these exhibited essentially identical features, which we interpreted to represent the characteristics of a charge free oxide. The plot of this spectrum on a logarithmic scale, also depicted in Fig. 5, again emphasizes the oscillatory structure immediately above the threshold of ~ 3.6 V. This value was obtained from computer-aided fits to the threshold region of many spectra.¹⁹ The obvious difference between the spectra for the two different oxide thicknesses is that the 30 Å oxide exhibits two more maxima over the same energy interval. This is

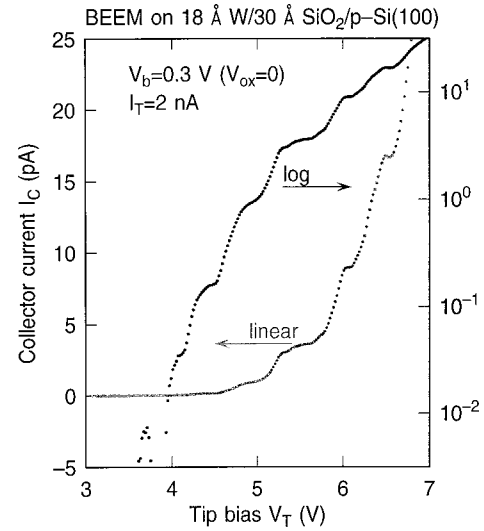


FIG. 6. Linear and logarithmic plot of a BEEM spectrum for a 18 Å W/30 Å SiO₂/p-Si(100) MOS sample. The logarithmic scale is shown on the right ordinate. $I_T = 2$ nA.

due to the increase in d_{ox} and can be readily understood by inspecting Eq. (1) for the ideal square barrier case. Taking the differential of Eq. (1), one gets

$$\Delta E/E = -2\Delta d_{ox}/d_{ox}. \quad (2)$$

Thus, an increase in d_{ox} results in a decrease in the energy separation of the maxima.

IV. TRANSMISSION PROBABILITIES AND FITTING PROCEDURE

The incorporation of screening effects and a more realistic treatment of the interfaces requires a numerical solution of the one-dimensional Schrödinger equation to calculate the energy dependent transmission probability T_{ox} . Only an outline will be presented here, as details can be found elsewhere.¹⁸ At the outset, we assume a parabolic dispersion of $E(k)$ in the oxide, with an effective mass m_{ox} as parameter. Consequently, the momentum takes the form

$$k(x) = \sqrt{2m_{ox}/\hbar^2} \sqrt{E - [\Phi_B + eF_{ox}x + E_{im}(x)]}, \quad (3)$$

where Φ_B is the barrier height, E_{im} is the image potential that includes the effect of all images in the two electrodes,⁷ and F_{ox} is the oxide field. The singularity of the classic image potential at the interfaces was “removed” by extending both the band edges in the semiconductor and the Fermi level in the metal until they intersect the image potential. We use the approach of Ando and Itoh for an arbitrary potential barrier by segmenting the barrier [such as depicted in Fig. 1(b)] into N equal intervals with coordinate x_1 marking the 1th segment.²⁴ With continuity of both wave function and quantum-mechanical current density as boundary conditions at each interface, $T_{ox}(E)$ is then expressed as

$$T_{ox}(E) = \frac{m_0}{m_{N+1}} \frac{k_{N+1}}{k_0} \frac{|\det M|^2}{|M_{22}|^2}, \quad (4)$$

where M is a (2×2) product matrix $M = \prod_{l=0}^N M_l$ with transfer matrices $M_l(x_l)$ being only functions of momentum k_l and effective mass m_l in the l th segment.²⁴ With the metal-oxide interface at x_0 and the oxide-silicon interface at x_N , $m_0 = m_M$ denotes the effective mass of the conduction electrons in the metal electrode and $m_N = m_{Si}$ the corresponding mass in silicon. For all other l we have $m_l = m_{ox}$. The following parameters were used in the simulations: (a) for both oxides: $N = 30$, $m_{Si} = 0.19m_0$, $m_M = m_0$, $\epsilon_{Si} = 11.7$ and $\epsilon_{ox} = 2.13$; (b) for the 23 Å oxide with Pd gates: $d_{ox} = 23$ Å, $\Phi_B = 4.01$ eV, $F_{ox} = V_{ox}/d = 0$ and 0.07143 V/nm (potential peak at the oxide-metal boundary).⁸ The finite value of the field corresponds to a $V_{ox} \approx 0.2$ V, and serves to assess the shifts in m_{ox} due to uncertainties in V_{ox} . (c) For the 30 Å with W gates: $d_{ox} = 30$ Å, $\Phi_B = 3.77$ eV, $F_{ox} = 0$. The value of Φ_B agrees well with the 3.7 eV value for a 76 Å oxide obtained from $I-V$ measurements (FM) on W-gated capacitor structures.²³

$T_{ox}(E)$ is a rapidly rising function for $E > eV_{th}$ that exhibits an oscillatory structure with maxima near unity,^{9,18,24} and need not be reproduced here. The initial observations of interference phenomena in BEEM were characterized by relatively noisy spectra that exhibited only 3–4 clearly distinguishable peaks, whose positions could be fitted theoretically with a single valued m_{ox} .¹⁹ A similar approach for the present multip peaked interference structure failed, however, and we had to resort to an energy dependent mass to match theory to experiment. The following procedure was used to match the theoretical interference maxima to the experimental data, an example of which is shown in Fig. 5 for the 23 Å oxide. With the parameters listed earlier, and m_{ox} as a variable, T_{ox} was numerically evaluated until agreement was obtained between the first theoretical and experimental peaks, thus yielding $m_{ox}(E_1)$. Then m_{ox} was increased until agreement was reached between the second theoretical and experimental peaks, yielding $m_{ox}(E_2)$. The same was done for all higher lying peaks, giving values $m_{ox}(E_i)$ at peak energies E_i by the best fit between theoretical and measured T_{ox} . $m_{ox}(E_i)$ defines a mass dispersion curve for the discrete peak energies E_i . Interpolation of $m_{ox}(E_i)$ between the peak energies results in a smooth mass dispersion $m_{ox}(E)$ with the property that the theoretical interference maxima match the measured interference peaks.

V. MASS DISPERSIONS AND DISCUSSION

For the indicated peak positions of the 23 Å oxide in Fig. 5 we have calculated $m_{ox}(E)$ under various assumptions related to uncertainties in the parameters. The results are shown in Fig. 7 plotted as a function of V_T . The solid curve represents the most likely dispersion using the best estimates for the values of the parameters, as given in Sec. IV. The symbols represent the calculated values, while the smooth curves are spline fits through the data points (for clarity we have omitted the data points in some curves). The dashed curve represents $m_{ox}(E)$ calculated from maxima obtained from the four averaged spectra shown in Fig. 4. As discussed earlier, uncertainties in the thickness have the largest effects

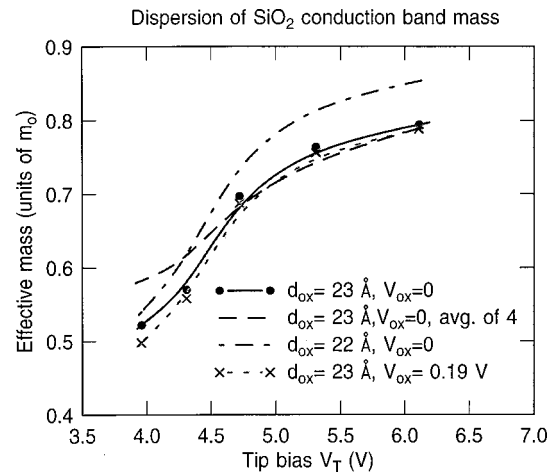


Fig. 7. Conduction band mass dispersions for a 23 Å oxide. The various curves depict $m_{ox}(E)$ calculated for variations in parameters for which the mass is particularly sensitive. The solid curve depicts the dispersion calculated with the best estimates for d_{ox} , Φ_B , and V_{ox} .

on m_{ox} . A change of 1 Å results in a rather large change in $m_{ox}(E)$, particularly at the higher energies, as shown by the dot-dashed curve in Fig. 7, which depicts the results for a decrease of 1 Å in the oxide to 22 Å. On the other hand, uncertainties in V_{ox} have a much smaller effect on the mass, as shown in Fig. 7 by the small change generated when V_{ox} is changed from 0 to 0.19 V (dotted curve). This value is outside an estimated uncertainty in V_{ox} of ± 0.1 V.

The calculated mass dispersion based on the data of Fig. 6 for the 30 Å oxide is shown in Fig. 8 by the lower solid curve. The dotted curve represents the same data, but assumes a decrease in thickness to 29 Å, as was done for the 23 Å oxide. The mass dispersion of the latter is again shown in the figure by the upper solid curve. The barrier height or threshold energy has been subtracted to obtain the kinetic

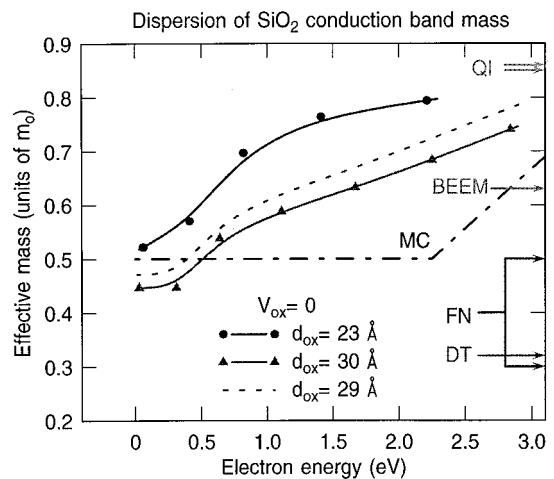


Fig. 8. Energy dispersions of the conduction band mass of SiO₂ for a 30 Å oxide (lower solid curve) and for a 23 Å oxide (upper solid curve). The dotted curve represents a reduction of 1 Å of the 30 Å oxide to $d_{ox} = 29$ Å, which shifts the dispersion upwards. Some previously reported values of m_{ox} are indicated along the right ordinate.

energy in the conduction band of the SiO₂. Because of the curvature in the barrier profile due to image effects, as shown in Fig. 1(b), the electron has a position dependent kinetic energy in the oxide. The abscissa in Fig. 8, due to the subtraction of V_{th} , thus corresponds to the minimum kinetic energy experienced by the electrons, with $m_{ox}(E)$ representing a weighted average over a range of energies. However, we observed previously that the average value for m_{ox} is only about 3% smaller than the mass calculated by excluding image force effects.¹⁸ The latter scenario, for $V_{ox}=0$, leads to a position independent kinetic energy. Thus, $m_{ox}(E)$ in Fig. 8 can be interpreted as representing to within a few percent the mass at the actual value of the kinetic energy.

It is clearly evident that an appreciable dispersion is observed in m_{ox} over the energy range to 3 eV. The expectation that m_{ox} disperses is not new,^{1,25} but had not previously been demonstrated experimentally. A “dispersion” marked MC in Fig. 8 has been used in Monte Carlo calculations of a variety of hot electron transport phenomena in SiO₂.^{19,25–27} A relevant question at this point concerns the disparity between the two curves for different oxide thickness: is there a real difference or can experimental uncertainties account for the difference? Because of the quadratic dependence of m_{ox} on d_{ox} an error in d_{ox} is doubled for m_{ox} , as is readily ascertained by differentiating Eq. (1) and obtaining $\Delta m_{ox}/m_{ox} = -2\Delta d_{ox}/d_{ox}$. This dominance of an uncertainty in m_{ox} outweighs that for the other parameters, as discussed earlier. The relative accuracy between the 23 and 30 Å oxides is within 1 Å, while their absolute thickness is estimated to have an uncertainty of ± 1 Å. Judging from the $C-V$ determined thicknesses that are about 1 Å smaller, the uncertainty should be weighted towards a smaller value of d_{ox} . However, assuming such an error, as represented by the dotted line for the 29 Å oxide in Fig. 8, it is thus unlikely that the difference in the two dispersions can be attributed to uncertainties in the values of d_{ox} . A second source of errors can arise from uncertainties in the determination of the interference maxima, as well as from small deviations between comparable spectra. However, comparing a single spectrum with an average of four spectra, shown as the dashed curve in Fig. 7, clearly shows that this possible source of error cannot account for the large differences observed for the different thickness. We therefore conclude that the 23 Å oxide exhibits a different, faster rising dispersive behavior than the 30 Å oxide. This difference may arise from band structure changes that result from an increased confinement in the direction normal to the film for the 23 Å oxide. Nevertheless, both curves show an initial slow change from a value near $0.5 m_0$ that implies, particularly for the 30 Å oxide, the presence of a parabolic conduction band. This observation is in agreement with the parabolic behavior at the bottom of the conduction band predicted for crystalline SiO₂.^{15–17}

Also indicated on the right margin of Fig. 8 are a number of values for m_{ox} reported in the literature. The range for FN determined values is shown for illustrative purposes only, as these values represent tunneling masses that are only indirectly related to the real conduction band mass. The two

values near $0.85 m_0$, marked QI, were obtained from quantum interference oscillations in FN experiments and were reported by Maserjian¹⁰ and by Zafar *et al.*⁴ The position labeled BEEM is from our earlier results for the 28 Å SiO₂ sample.¹⁸ Its value of $0.63 m_0$, based on a single mass fit of the interference structure, thus represents an average over the energy interval, and is in excellent agreement with an average m_{ox} for the 30 Å oxide. The question now arises as to why the QI results from the FN experiments are substantially larger than the range of values obtained with BEEM. Before addressing this point, it is instructive to briefly discuss the differences in the techniques and the critical parameters that enter in the determination of m_{ox} . Aside from BEEM being a local and FN a broad area probe, the crucial difference lies in the nearly monoenergetic nature of BEEM injected electrons²⁸ that maintain a relatively constant kinetic energy in the oxide, as opposed to the continuously changing energies of FN injected electrons. In order to observe interference phenomena the field has to be changed in FN measurements, which changes the injection conditions, i.e., cavity length, image force effects and current, with the consequence that the interference signal represents an energy averaged, relatively weak component modulating an exponentially increasing background current. Whereas the deduction of m_{ox} by BEEM depends crucially only on one parameter, namely the thickness d_{ox} , and to a substantially lesser extent on Φ_B and V_{ox} ,¹⁸ the precise knowledge of all three parameters is critical for the FN determination of m_{ox} .⁴ The latter depends, as for over-the-barrier injection in BEEM [Eq. (1)] on the inverse square of d_{ox} , but more significantly, on the inverse cube of Φ_B .⁴ The effective barrier height is affected by the image force lowering that is significantly more pronounced at high fields (Schottky effect^{8,29}) assuming, of course, that its zero field value is accurately known to begin with, itself a questionable assumption. For BEEM determined masses it was estimated that at relatively low fields of $\sim 6.8 \times 10^5$ V/cm, the increase in the average mass due to image force neglect is about 3%.¹⁸ The increases should be substantially larger in the FN experiments, for which the fields are 20-fold higher. Another contribution to experimental uncertainty is oxide charge, which affects the net oxide field, a problem that we assiduously avoided in BEEM through selective choice of local injection sites. The presence of positive oxide charge was reported,^{3,10} and constitutes a nearly unavoidable problem in low level stressing of SiO₂.³⁰ Its effect further lowers the barrier height, as depicted by the dashed potential profile in Fig. 1(b).

VI. CONCLUDING REMARKS

We have further demonstrated here the versatility and power of the highly localized hot electron capabilities of BEEM. The relatively simple physical concept and formulation of the monochromatic over-the-barrier electron current was used here to obtain for the first time the energy dispersion of the effective mass of conduction band electrons in SiO₂. A thickness dependence was also observed, with the thinner 23 Å oxide exhibiting a larger mass than the 30 Å

oxide, although the net changes in dispersion were comparable over the same energy range. Since this difference was outside the estimated uncertainties in the thicknesses of the oxides, a primary source for error in determining m_{ox} , it was intimated that the thickness of the 23 Å oxide was sufficiently small to affect deviations from bulk-like features of the band structure. The validity of this conjecture could be assessed through an appropriate band structure calculation. The observed range of dispersion from ~ 0.5 to $\sim 0.8 m_0$ is substantially larger than the tunneling masses deduced from direct tunneling and FN experiments, although an agreement exists at the low kinetic energy value. However, these masses should not be confused, as frequently done in the literature. Due to experimental constraints of FN measurements, the electron masses are at best averaged values that are obtained from fits of data to simple analytic expressions that neglect several relevant physical phenomena. It is hoped that modeling sophistication will overcome this problem, and that at one point in the future it will be feasible as well to determine the dispersion of the tunneling mass.

ACKNOWLEDGMENTS

The authors acknowledge many fruitful discussions with Ed Cartier. Special thanks go to both Doug Buchanan, for the $C-V$ thickness measurements, and to Chris D'Emic for growing the oxide samples, as well as for the ellipsometric thickness measurements.

¹M. V. Fischetti, S. E. Laux, and E. Crabbé, *J. Appl. Phys.* **78**, 1058 (1995), and references therein.

²T. Yoshida, D. Imafuku, J. L. Alay, S. Miyazaki, and M. Hirose, *Jpn. J. Appl. Phys., Part 2* **34**, L903 (1995).

³J. Maserjian and G. P. Petersson, *Appl. Phys. Lett.* **25**, 50 (1974).

⁴S. Zafar, K. Conrad, Q. Liu, E. A. Irene, G. Hames, R. Kuehn, and J. J. Wortman, *Appl. Phys. Lett.* **67**, 1031 (1995).

⁵M. Lenzlinger and E. H. Snow, *J. Appl. Phys.* **40**, 278 (1969).

⁶Z. A. Weinberg and A. Hartstein, *Solid State Commun.* **20**, 179 (1976).

⁷A. Schenk and G. Heiser, *J. Appl. Phys.* **81**, 7900 (1997).

⁸H. J. Wen, R. Ludeke, D. M. News, and S.H. Low, *J. Vac. Sci. Technol. A* **15**, 784 (1997).

⁹K. H. Gundlach, *Solid-State Electron.* **9**, 949 (1966).

¹⁰J. Maserjian, *J. Vac. Sci. Technol.* **11**, 996 (1974).

¹¹M. V. Fischetti, D. J. DiMaria, L. Dori, J. Batey, E. Tierney, and J. Stasiak, *Phys. Rev. B* **35**, 4044 (1987).

¹²J. C. Poler, K. K. McKay, and E. A. Irene, *J. Vac. Sci. Technol. B* **12**, 88 (1994).

¹³S. Zafar, Q. Liu, and E. A. Irene, *J. Vac. Sci. Technol. A* **13**, 47 (1995).

¹⁴H. S. Momose, M. Ono, T. Yoshitomi, T. Ohguru, S. Nakamura, M. Saito, and H. Iwai, *IEEE Trans. Electron Devices* **45**, 1233 (1996).

¹⁵P. M. Schneider and W. B. Fowler, *Phys. Rev. Lett.* **36**, 425 (1976); *Phys. Rev. B* **18**, 7122 (1978).

¹⁶J. R. Chelikowsky and M. Schlüter, *Phys. Rev. B* **15**, 4020 (1977).

¹⁷Y.-N. Xu and W. Y. Ching, *Phys. Rev. B* **44**, 11048 (1991).

¹⁸H. J. Wen, R. Ludeke, and A. Schenk, *J. Vac. Sci. Technol. B* **16**, 2296 (1998); R. Ludeke, H. J. Wen, and A. Schenk, *Appl. Phys. Lett.* **73**, 1221 (1998).

¹⁹R. Ludeke, A. Bauer, and E. Cartier, *J. Vac. Sci. Technol. B* **13**, 1830 (1995); *Appl. Phys. Lett.* **66**, 730 (1995).

²⁰R. Ludeke, H. J. Wen, and E. Cartier, *J. Vac. Sci. Technol. B* **14**, 2855 (1996).

²¹R. Ludeke and M. Prietsch, *J. Vac. Sci. Technol. A* **9**, 885 (1991).

²²H. J. Wen and R. Ludeke, *J. Vac. Sci. Technol. A* **16**, 1735 (1998).

²³D. A. Buchanan, F. R. McFeely, and J. J. Yurkas, *Appl. Phys. Lett.* **73**, 1676 (1998).

²⁴Y. Ando and T. Itoh, *J. Appl. Phys.* **61**, 1497 (1987).

²⁵M. V. Fischetti, D. J. DiMaria, L. Dori, J. Baty, E. Tierney, and J. Stasiak, *Phys. Rev. B* **35**, 4404 (1987).

²⁶E. Cartier and F. R. McFeely, *Phys. Rev. B* **44**, 10689 (1991).

²⁷D. Arnold, E. Cartier, and D. J. DiMaria, *Phys. Rev. B* **49**, 10278 (1994).

²⁸N. D. Lang, A. Yacoby, and Y. Imry, *Phys. Rev. Lett.* **63**, 1499 (1989); N. D. Lang (unpublished).

²⁹S. M. Sze, *Physics of Semiconductor Devices*, 2nd ed. (Wiley, New York, 1981).

³⁰D. A. Buchanan, D. J. DiMaria, C.-A. Chang, and Y. Taur, *Appl. Phys. Lett.* **65**, 1820 (1994).